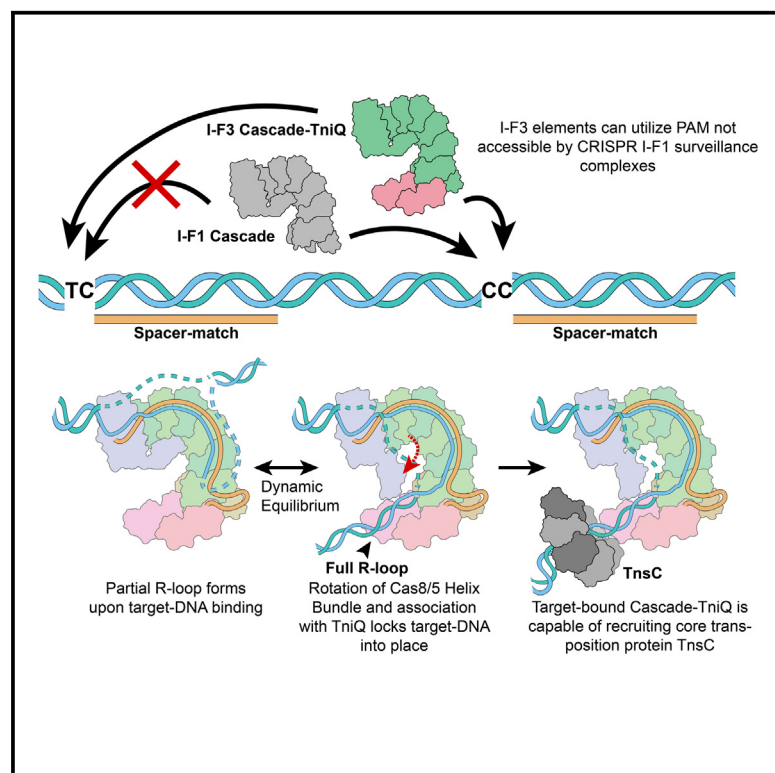**Article**

Multiple adaptations underly co-option of a CRISPR surveillance complex for RNA-guided DNA transposition

Graphical abstract

Authors

Jung-Un Park, Michael T. Petassi, Shan-Chi Hsieh, ..., Ailong Ke, Elizabeth H. Kellogg, Joseph E. Peters

Correspondence

lizkellogg@gmail.com (E.H.K.),
joe.peters@cornell.edu (J.E.P.)

In brief

Park et al. investigate the mechanisms of the DNA-recognition module from I-F3 CRISPR-Cas-associated transposons, Cascade-TniQ. They demonstrate that TniQ functions in target engagement and regulation of target-site choice with Cascade components. Comparing PAM recognition of I-F3 Cascade with canonical CRISPR-Cas reveals the structural basis of PAM ambiguity.

Highlights

- Structures of I-F3 CAST effector module reveal roles of transposon protein TniQ

- TniQ participates in complete R-loop formation by engaging with target DNA

- TniQ regulates target-site choice through interactions with crRNA

- Structural basis of PAM ambiguity in I-F3 CAST compared with canonical CRISPR-Cas

CellPress

Article

Multiple adaptations underly co-option of a CRISPR surveillance complex for RNA-guided DNA transposition

Jung-Un Park,[1,4] Michael T. Petassi,[2,4] Shan-Chi Hsieh,[2,4] Eshan Mehrotra,[1,4] Gabriel Schuler,[1] Jagat Budhathoki,[1] Vinh H. Truong,[1] Summer B. Thyme,[3] Ailong Ke,[1] Elizabeth H. Kellogg,[1,*] and Joseph E. Peters[2,5,*]

[1]Department of Molecular Biology and Genetics, Cornell University, Ithaca, NY 14853, USA
[2]Department of Microbiology, Cornell University, Ithaca, NY 14853, USA
[3]Department of Neurobiology, The University of Alabama at Birmingham, Birmingham, AL 35294, USA
[4]These authors contributed equally
[5]Lead contact
*Correspondence: lizkellogg@gmail.com (E.H.K.), joe.peters@cornell.edu (J.E.P.)
https://doi.org/10.1016/j.molcel.2023.05.005

SUMMARY

CRISPR-associated transposons (CASTs) are natural RNA-directed transposition systems. We demonstrate that transposon protein TniQ plays a central role in promoting R-loop formation by RNA-guided DNA-targeting modules. TniQ residues, proximal to CRISPR RNA (crRNA), are required for recognizing different crRNA categories, revealing an unappreciated role of TniQ to direct transposition into different classes of crRNA targets. To investigate adaptations allowing CAST elements to utilize attachment sites inaccessible to CRISPR-Cas surveillance complexes, we compared and contrasted PAM sequence requirements in both I-F3b CAST and I-F1 CRISPR-Cas systems. We identify specific amino acids that enable a wider range of PAM sequences to be accommodated in I-F3b CAST elements compared with I-F1 CRISPR-Cas, enabling CAST elements to access attachment sites as sequences drift and evade host surveillance. Together, this evidence points to the central role of TniQ in facilitating the acquisition of CRISPR effector complexes for RNA-guided DNA transposition.

INTRODUCTION

CRISPR-associated transposons (CASTs) have gained substantial interest due to their capacity to direct a single-cargo DNA insertion at a pre-programmed position.[1] These transposition systems can be highly complex: in addition to 3–4 conserved transposition genes, they encode one or more CRISPR-Cas domain proteins from independent CRISPR effector subtypes.[2] The largest group of sequenced CAST elements derived from type I-F1 CRISPR-Cas systems, referred to as type I-F3 CAST elements. These fall primarily into two large branches, I-F3a and I-F3b, that exhibit differences in both CRISPR array configuration and regulation.[3]

Type I-F3 CASTs have evolved mechanisms to target transposition in two classes of target sites, akin to prototypic Tn7 and other elements within the larger Tn7-like transposon family: (1) mobile elements and (2) a conserved position in the bacterial chromosome adjacent to an essential gene known as the attachment site.[2,4] These two pathways facilitate the horizontal transfer of the transposon to new bacterial hosts by parasitizing the mobilization capabilities of targeted plasmids and bacteriophage. All I-F3 CASTs use CRISPR RNAs (crRNAs) encoded within a standard array to target transposition into mobile elements but have evolved different adaptations to direct transposition into the attachment site in the two major I-F3 branches. The I-F3a elements have two CRISPR arrays that are differentially regulated. One array is expressed only when the element enters a naïve host.[3] This array encodes a single crRNA that recognizes a conserved chromosomal attachment site. A second array encodes crRNAs that primarily recognize mobile plasmids. The I-F3b elements maintain a single array, but the final crRNA encoded in the array is functionally different, possessing a repeat sequence that is different from the other repeats in the array, called an atypical crRNA. The sequence differences between typical and atypical crRNA repeats have been described previously.[3] The atypical crRNAs are found with spacers that recognize a conserved chromosomal attachment site, which in the I-F3b branch corresponds to the *ffs* gene encoding the RNA component of the signal recognition particle protein translocation system. The I-F3b effector complex recognizes both typical and atypical crRNAs, but an unknown mechanism allows a higher frequency of transposition with atypical crRNAs. This process therefore allows crRNAs to be categorized by favoring transposition into the *ffs* attachment site in the chromosome.
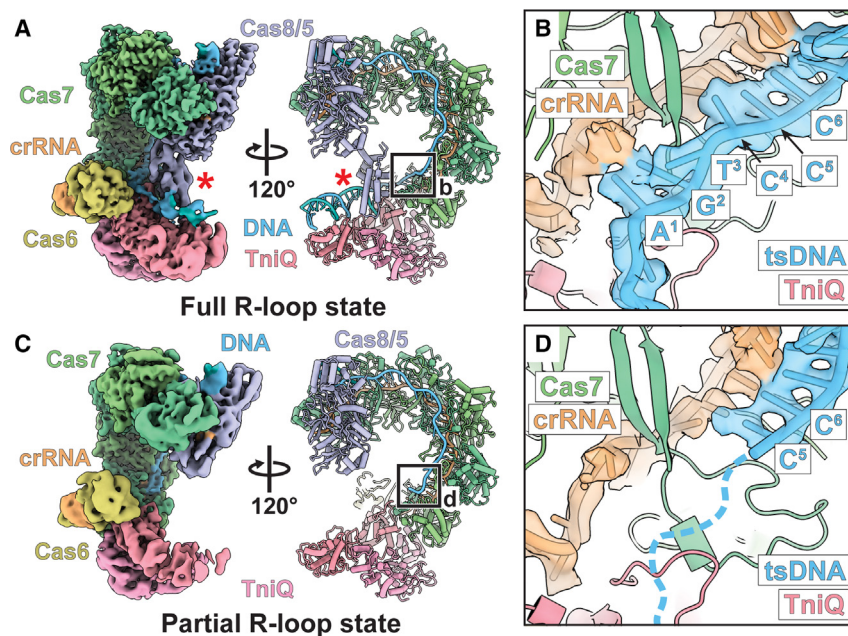
Figure 1. High-resolution cryo-EM reveals full R-loop and partial R-loop states of the DNA-bound Cascade-TniQ complex

(A) Cryo-EM reconstructions and atomic model of the Cascade-TniQ complex in the full R-loop state (fully engaged RNA-DNA hybrid). The complex includes the following components: Cas8/5 (purple), Cas7 (green), Cas6 (yellow), CRISPR RNA (crRNA, orange), TniQ (pink), and target DNA (blue). Red asterisks (*) indicate the Cas8/5 helix bundle domain. Black box defines the region for the close-up view in (B). Local-resolution filtered maps from the focused refinements were combined for visualization (see STAR Methods).

(B) Close-up view of the cryo-EM density and the atomic model of crRNA and target-strand DNA (tsDNA) from the full R-loop state conformation. The cryo-EM reconstruction visualizes the full engagement of tsDNA to crRNA.

(C) Cryo-EM structure of the Cascade-TniQ complex in the partial R-loop state. Color scheme is identical to (A). Black box indicates the region for detailed view in (D).

(D) Close-up view of PAM-distal region of the R-loop from the cryo-EM structure of partial R-loop state. Base pair positions one through four are not resolved in the cryo-EM reconstruction of the partial R-loop conformation, indicated with dashed lines.

The mechanistic basis of this ability to discriminate between crRNAs nor which CRISPR-Cas or transposition proteins might serve to discriminate between crRNA categories is unknown. To address this question, we focused our attention on components known to contact the crRNA, Cascade components, and TniQ. Previous cryoelectron microscopy (cryo-EM) studies of a I-F3a element revealed a direct physical association between the CRISPR effector (referred to throughout as the Cascade complex) and conserved transposon protein TniQ,[5] which serves to recruit downstream transposition machinery. TniQ interacts with a AAA+ regulator, TnsC, to recruit the heteromeric transposase, TnsA and TnsB.[4] All target-bound Cascade-TniQ complexes from I-F3 CAST systems examined to date exhibit incomplete R-loop formation,[5–7] even when reconstituted with DNA substrates designed to promote R-loop formation.[8] Therefore, it remained unclear whether additional transposition components or unknown host factors were required for full R-loop formation and how they might engage the effector complex.

To investigate the molecular adaptations associated with CAST element evolution as well as mechanistically characterize the initial stages of CAST transposition, we examined the structure of DNA-bound type I-F3b CRISPR effector complex, Cascade-TniQ. Our work reveals multiple previously unappreciated roles for TniQ in licensing transposition, acting to distinguish between typical and atypical crRNA categories, and as a platform for the recruitment of downstream transposition components (akin to TnsD from prototypic Tn7; see Discussion). Finally, we characterize mechanisms allowing I-F3b CAST elements to develop protospacer adjacent motif (PAM) ambiguity for host immune surveillance escape and to tolerate diversification of attachment sites recognized by the system.

RESULTS

Cryo-EM reveals structural requirements for full R-loop engagement

We used cryo-EM to structurally characterize the I-F3b element (Tn6900) Cascade complex (including proteins Cas6, Cas7, and Cas8/5 in yellow, green, and purple shown in Figure 1A) associated with the TniQ transposition protein (pink) and target DNA (blue, Figures 1A and S1). The overall architecture of the I-F3b Cascade-TniQ complex closely matches previously published I-F3a cryo-EM structures.[5] As a result of the conformational dynamics present within the complex, 3D reconstruction of the particle stack before classification (overall assessed to be 3.2 Å average resolution) contained comparatively weak TniQ density and variable local resolution throughout the structure (Figure S1). Nevertheless, we were able to capture two class averages, one with a full R-loop (Figures 1A and 1B) and one with a partial R-loop, in which incomplete target-DNA density is observed at the PAM-distal end of the complex (Figures 1C and 1D). The full R-loop structure showed cryo-EM density for the entire crRNA-hybridized 32-bp target strand (TS) (Figure 1B), as well as the density for the PAM-distal DNA (Figure 1A). On the other hand, the partial R-loop structure visualized only 28 bp of the TS annealed with crRNA (Figure 1D). 3D variability analysis (3DVA)[9] revealed that the dominant motion (i.e., separable using the first eigenvector) is the result of breathing motions in the complex separating partially bound target DNA and fully engaged R-loop conformations (see Video S1). Full R-loop formation is accompanied by a 90° rotation of the Cas8/5 fused helix bundle domain (red asterisk, Figure 1A; Video S1); a domain missing from prior I-F3a structures,[5] which more
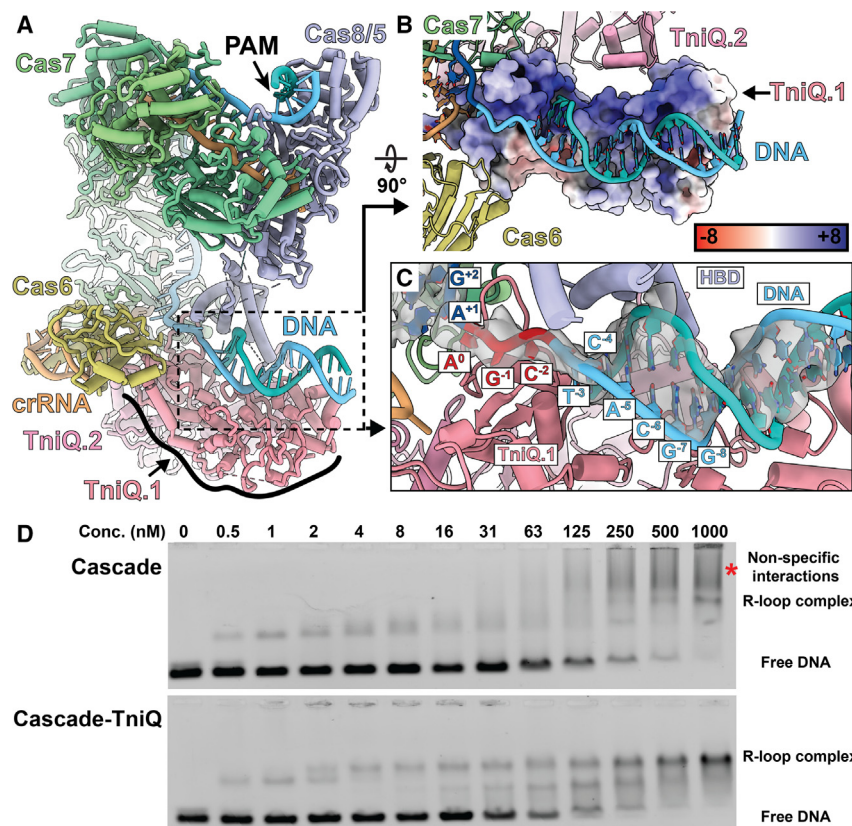
Figure 2. PAM-distal end of target DNA in full R-loop state is further unwound, interacting with TniQ and Cas8/5 helix bundle domain

(A) Atomic model of a full R-loop formed Cascade-TniQ complex, shown for reference. The color scheme is consistent with Figure 1A. TniQ is distinguished by numbers (TniQ.1 or TniQ.2) to indicate which subunit interacts with the target DNA.

(B) One TniQ subunit (TniQ.1, surface representation) interacts with the PAM-distal DNA duplex (blue). DNA binding region of TniQ surface is positively charged, represented by the positive electrostatic potential. Legend indicates the color key for the dimensionless electrostatic potential calculated by APBS. Information for this software is in the Software and algorithms section.

(C) The PAM-distal target DNA is unwound by additional three base pairs (red) following the protospacer (dark blue). Downstream double-stranded DNA interacts with the Cas8/5 helix bundle domain (HBD, purple) and TniQ.1 subunit.

(D) Electrophoretic mobility shift assay (EMSA) reveals that TniQ promotes R-loop formation of Cascade with target DNA. At low concentrations, Cascade without TniQ shifts the DNA in a similar manner as Cascade-TniQ, but it forms a smeary band at high concentrations (≥250 nM, indicated with a red asterisk). On the other hand, Cascade associated with TniQ forms discrete bands in EMSA. The binding configurations that correspond to the band positions are indicated on the right of the gel image.

closely resembles the partial R-loop structure (Figure 1C). This rotation is correlated with a slight expansion of the Cascade complex (Video S1). The observed conformational change is reminiscent of a similar conformational change in type I-F1 Cascade, in which the helical bundle of Cas8f rotates roughly 180° on target-DNA binding.[10] The conformational change we observe in the I-F3b particle population is tightly correlated with R-loop formation, which suggests that this is required prior to recruitment of downstream transposition factors (i.e., TnsC).

It was previously suggested that Cascade-TniQ might require other transposition components (i.e., TnsABC) for complete R-loop formation,[5] Although we cannot rule out the possibility that another factor is required to stabilize association as shown in other Tn7-like transposons[11] including the V-K CAST system,[12] the structure presented implies that Cascade-TniQ itself is sufficient to form a full R-loop without additional host factor or transposition components. PAM-distal duplex DNA was not observed in previously determined I-F1 CRISPR-Cas structures,[10] suggesting that, in this case, TniQ may serve as an additional platform in this system for stabilizing the distal end of the R-loop preparing the DNA substrate for transposition initiation. Although TniQ is associated with Cascade as a homodimer, only one monomer of TniQ (TniQ.1) associates with target DNA, which follows a path roughly parallel to the dimerization interface of TniQ (Figures 2A and 2B). Another TniQ subunit (TniQ.2) does not engage with the target DNA, potentially serving a structural role in the complex. The TniQ surface in

contact with DNA is highly basic (Figure 2B) and has a footprint that spans 18 base pairs (bp) (Figure S2A). We also observed distortion in the PAM-distal DNA corresponding to a slight lengthening and duplex DNA unwinding (Figure S2B). Although the local resolution of this region is slightly worse (5–6 Å) compared with the average resolution of the cryo-EM map (3.5 Å, Figure S1), the modeled substrate fits the cryo-EM map substantially better than an ideal B-form DNA model (cross-correlation is 0.71 vs. 0.22 for distorted compared with ideal DNA). The DNA distortion is further accompanied by unwinding of approximately 3 base pairs past the expected protospacer region (colored red, Figure 2C), modeling which is supported by the model-map Fourier shell correlation (FSC) (3.5 vs. 3.7 Å for the gold-standard vs. model-map FSC, respectively).

We propose a model in which the Cascade-TniQ complex presents target DNA for TnsC recruitment. Based on these structural observations (Figures 2A–2C), we reasoned that TniQ may have a second, previously unappreciated role in stabilizing R-loop formation. To test this hypothesis, we probed the extent of R-loop formation by comparing the DNA binding of purified Cascade and Cascade-TniQ complexes using electrophoretic mobility shift assays (EMSAs) (Figures 2D and S3A). We titrated fluorescently labeled target DNA (0.5 nM) with Cascade or Cascade-TniQ complex. We found similarly shifted products at low concentrations of Cascade or Cascade-TniQ complex (<2 nM), suggesting that the initial DNA engagement with both complexes may be similar. However, at high

concentrations of Cascade, most of the DNA substrate shifts to slower-migrating, smeared bands, suggesting non-specific binding (most prominent at 1,000 nM, red asterisk on Figure 2D). Conversely, increasing concentrations of Cascade-TniQ complex exhibited substantially less non-specific binding than Cascade alone, instead resulting in two additional bands (Figure 2D). This suggests that different DNA-bound conformational states are present. To determine which band represents the full R-loop state, we conducted additional EMSA using pre-bubbled target-DNA-containing mismatched bases over the 32 bp protospacer sequence (Figure S3B). We reasoned that this pre-bubbled substrate would facilitate R-loop formation by reducing the energy required to melt the double-stranded DNA. We found that although the Cascade-TniQ resulted in both upper and lower bands with double-stranded target DNA, it formed only the upper band with pre-bubbled target DNA. This suggests that the upper band represents the full R-loop conformation. We speculate that the lower band may represent a partial R-loop state or another conformational state we have not captured in our cryo-EM analysis. Taken together, the EMSA data support the cryo-EM findings, indicating that TniQ is required to allow the I-F3 Cascade to form a stable R-loop product.

TniQ is responsible for crRNA category discrimination

Type I-F Cascade engages with a 60 bp crRNA, including a 32 bp spacer-derived sequence (orange, Figures 3A and 3B) flanked by an 8 bp 5′ handle (bound by Cas8/5, indicated with a purple arrow, Figures 3A and 3B) and a 20 bp 3′ stem-loop recognized by Cas6 (indicated with a yellow star, Figures 3A and 3B). The sequences of typical and atypical crRNA of I-F3b CAST contain major differences in the 5 nucleotides adjacent to the 3′ stem-loop ([41]GUGAA[45] and [41]AUUUU[45] for typical and atypical crRNA, respectively) (Figure 3C). Closer inspection of this region of crRNA reveals differences between the I-F3a (PDB: 6PIJ; Figure 3C left in light blue)[5] and I-F3b structures (this study, Figure 3C right in orange). In the I-F3a structure, the crRNA is too distant to make substantial interactions with TniQ (Figure 3C, left). However, the crRNA in the I-F3b structure reported here adopts a different path, with three bases (U42, U43, and U44) sufficiently close to interact with TniQ (2.9, 3.7, and 3.9 Å for U42, U43, and U44 respectively; Figure 3C right). This suggested that the molecular mechanisms for discriminating between different crRNA sequences (i.e., typical vs. atypical, as reported previously[3]) may originate from TniQ.

From this observation, we identified multiple basic TniQ residues in the general vicinity of the crRNA.[3] Although we did not observe specific interactions with RNA, we nevertheless sought to ascertain a potential functional role of either TniQ or Cas6 in discriminating crRNAs. Surprisingly, alanine mutations of crRNA-proximal residues in either TniQ (N283, R330, H384, and H387) or Cas6 (F113 and F153) increase the transposition activity of typical crRNA close to the activity of atypical crRNA (Figure 3E), indicating defects in the mechanism allowing regulation of crRNA preference. These findings demonstrate that TniQ plays an important role in modulating crRNA preferences with I-F3b CAST elements.[3]

Comparative analysis of I-F3b PAM and I-F1 PAM requirements for transposition and interference

Canonical I-F1 systems generally require a non-TS (NTS) CC PAM for interference activity.[13] In contrast, previous work by multiple groups has highlighted expanded PAM flexibility with I-F3 CAST systems compared with the canonical I-F1 CRISPR-Cas defense systems.[3,14–19] As part of our comparative analysis, we performed an unbiased PAM screen utilizing a target plasmid pool randomized at the PAM sequence ("−2" and "−1" positions; Figure 4A) associated with a plasmid-encoded *ffs* target sequence that is natively used as an attachment site for most of the I-F3b systems (Figure 4A). The target plasmid with the randomized PAM was then transformed into a cell population expressing the I-F3b Tn6900 CAST system or the 1-F1 *Pseudomonas aeruginosa* PA14 CRISPR-Cas defense system (Figure 4A). The transposition potential of all possible PAM combinations (4^2) was assessed by looking for PAM sequence enrichment in the population of plasmids that were targeted for transposition (Figure 4B) or PAM sequence depletion for targets subject to interference (Figure 4C) when compared with input plasmid population.

As expected, based on previous results,[13] the I-F1 interference system had a strong preference for CC, which was completely depleted from the pool (i.e., "<0.005" in Figure 4C). More generally, I-F1 interference activity depleted plasmids with a C in the −1 position (Figure 4C). By contrast, in the I-F3b transposition screen, we observe an overall loosening of PAM requirements (Figure 4B). Although the CC PAM did show a 3-fold enrichment as a transposition target (Figure 4B), all of the PAM combinations in the pool were used as transposition targets, with at most a modest <10-fold reduction for the least favored AA PAM (Figure 4B). To further validate these results, a subset of PAM sequences was individually constructed and tested in the mate-out transposition assay for I-F3b CAST (Figure 4D) or interference assay for I-F1 CRISPR-Cas (Figure 4E). Although the CC PAM was efficiently used as a target for transposition, many additional PAM combinations could be recognized as transposition targets, often only differing by a few percent in their transposition efficiency. This was markedly different than the result found with the interference assay with an almost two order of magnitude difference being found between the appropriate CC PAM and any of the other PAM combinations (Figures 4D and 4E).

Molecular basis of I-F3 CAST PAM promiscuity and specificity

Close inspection of structures representing the I-F1 CRISPR-Cas associated Cascade complex (PDB: 6NE0)[10] and the I-F3b CAST-associated Cascade-TniQ complex reveals candidate residues that could explain PAM sequence preferences (Figures 5A and S4A). Notably, serine residues S248 (3.6 Å) and S130 (2.2 Å) are within the hydrogen-bonding distance of the −1 and −2 PAM bases, respectively, in the I-F3b CAST structure (Figure 5A). In comparison, the −1 and −2 PAM bases in the I-F1 CRISPR-Cas structure interact with N250 and N111, respectively (Figure 5B). Serine residues are generally thought to be less specific in recognizing base sequences compared with asparagine, due to its limited ability to form bidentate interactions.[20] To explore the level of PAM specificity in the I-F3b system and validate the mechanisms suggested by our structural comparisons, we made
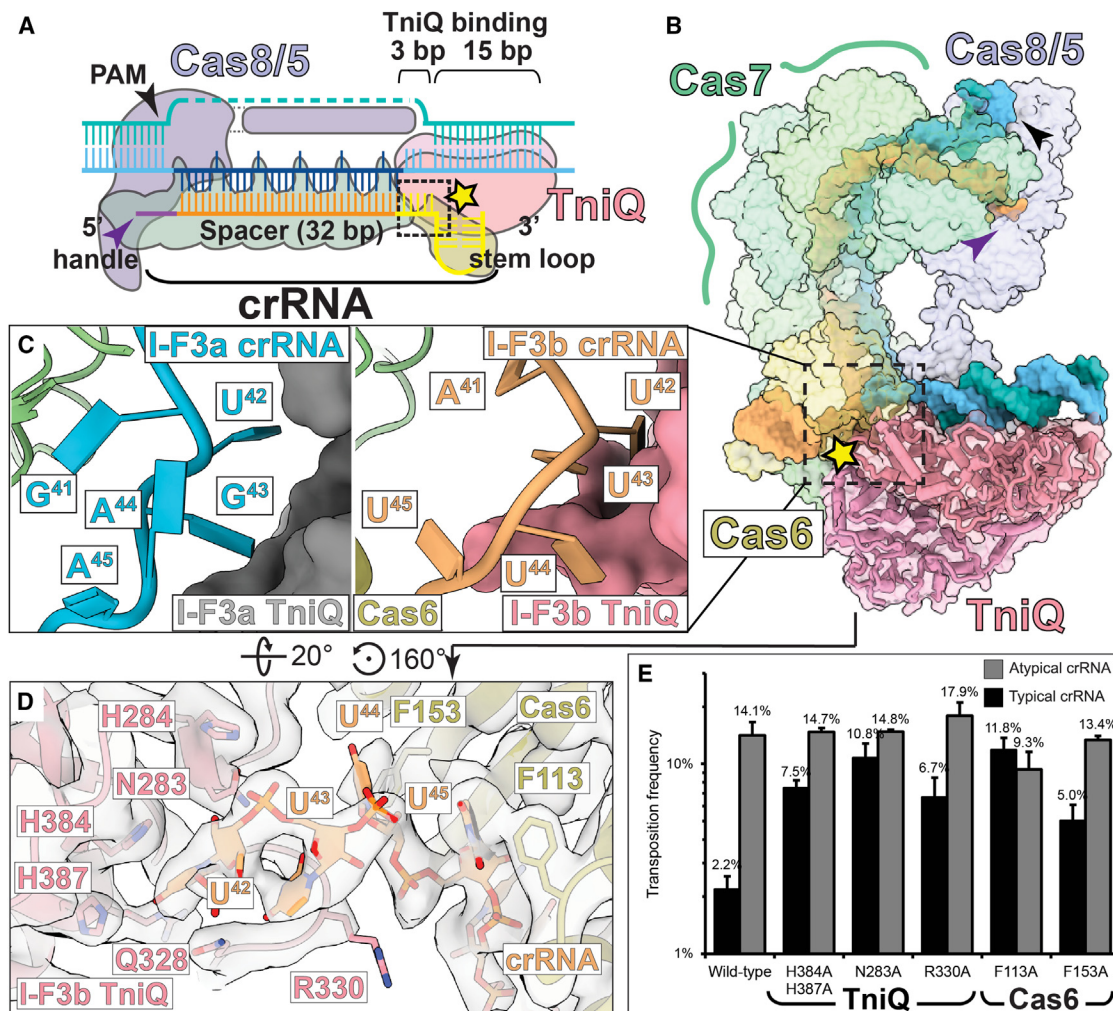
Figure 3. Comparison of the crRNA bound structure of I-F3a and I-F3b point to a regulatory mechanism enacted by TniQ

(A) Schematic of crRNA and target-DNA bound to Cascade-TniQ. Purple and black arrow indicate 5′ handle and PAM, respectively. Spacer and 3′ stem-loop of crRNA are colored orange and yellow, respectively. Black dashed box and yellow star indicate the interface between TniQ and crRNA.

(B) Structure of crRNA and bound DNA shown in opaque surface, protein shown in transparent surface. Dotted box indicates the region shown superimposed in (C). Symbols are as indicated in (A).

(C) Comparison of target-DNA-bound structures of the I-F3a (PDB: 6PIJ, left) and I-F3b (this study, right) reveals striking differences in the structure of crRNA (blue for I-F3a, orange for I-F3b).

(D) The I-F3b atomic model built into the cryo-EM density (transparent) reveals potential residues that may form the basis of the regulatory function of TniQ.

(E) *In vivo* transposition frequency with TniQ and Cas6 mutants compared with wild type with typical or atypical crRNA was monitored using the mate-out assay. Mutation of several crRNA-interacting residues abrogates the ability of I-F3b elements to regulate transposition as indicated by a restoration of typical crRNA transposition activity relative to atypical crRNA; data indicate mean ± standard deviation (n = 3 biological replicates).

changes in the S248 residue predicted to interact with the −1 position of the PAM (Figure 4A). We focused on this position as the I-F1 and I-F3b systems show a major difference in the PAM preference at the −1 position (Figures 4B and 4C). Interestingly, neither the S248N nor the S248A mutants could re-establish any substantial level of PAM discrimination (Figure 5C). This indicates that PAM specificity may depend on other energetic effects besides the identified contacts or it would require a more extensive change in the local environment than just the amino acid that directly interacts with the PAM to affect the positioning of residues involved in these contacts.

To address if the local environment that positions the S248 residue was also important for PAM discrimination, we tested double mutations at A247 and S248 residues. We generated two mutants that mimic the local environment of Cas8/5 from the I-F3a family (A247T + S248N; Figure S4B) or Cas8f from I-F1 Cascade (A247Q + S248N). Interestingly, the changes involving the residue S248N contacting the PAM and an adjacent residue increased sequence specificity at the −1 position to bias transposition to PAMs with a C at the −1 position, especially with the A247Q + S248N mutant resembling I-F1 Cas8f (Figures 5B and S5). Unlike wild-type Cas8/5 or the other mutants we
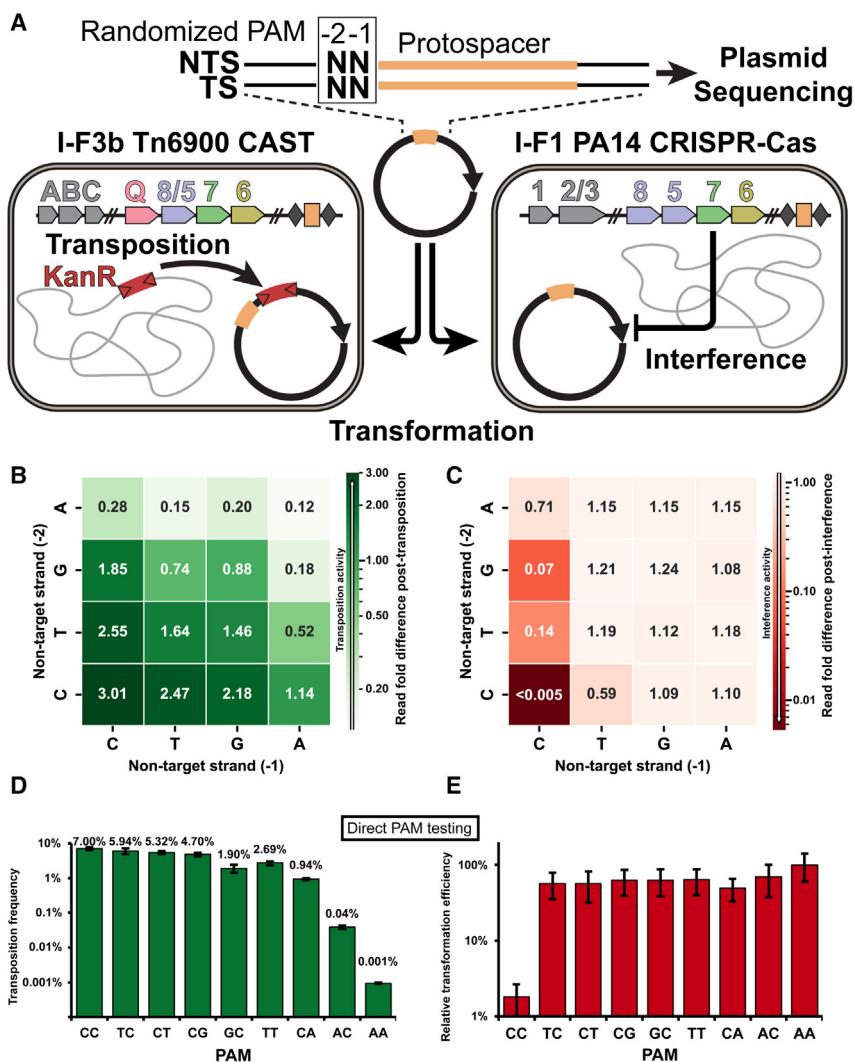
Figure 4. PAM requirement for I-F3b CAST transposition is more promiscuous than I-F1 CRISPR-Cas interference

(A) Schematic describing the workflow of the assay. Target plasmid with 2 base pair degenerate sequence upstream protospacer (orange) was sequenced before and after selection for transposition with I-F3b Tn6900 CAST or interference with I-F1 *P. aeruginosa* PA14 CRISPR-Cas.

(B) Heatmap indicating PAM sequence enrichment/depletion score following selection for Tn6900 transposition of sixteen possible PAM sequences. Values >1 indicate preferred PAMs more abundant after selection for transposition; values <1 are less preferred than average.

(C) Sequence enrichment/depletion with PA14 interference is shown as in (B). A lower score indicates higher interference activity.

(D and E). A subset of PAM sequences tested directly for transposition frequency in a mate-out assay (D) or interference activity by a transformation assay, with relative transformation efficiency compared to a non-target control plotted (E). Data indicate mean ± standard deviation (n = 3 biological replicates).

diversification of attachment sites recognized by the system (see discussion).

DISCUSSION

We find that co-option of type I-F Cascade for crRNA-directed transposition involved extensive reconfiguration of the control of the CRISPR-Cas effector. Our high-resolution structure reveals a series of new interactions between downstream DNA and both TniQ and as well as the Cas8/5 helix bundle domain (Figures 1 and 2). We propose that the new TniQ interactions we identify in the full R-loop complex reveal an important step for licensing a target for transposition in these systems (Figures 1 and 2). Additionally, these TniQ-DNA contacts result in a DNA distortion predicted to help accommodate TnsC-mediated transposase recruitment based on previous work with prototypic Tn7 (Figure 3).[21,22] We show that TniQ acts to mediate crRNA selection, sorting typical and atypical crRNAs to regulate target choice in the system (Figure 3). A direct comparison between PAM usage in I-F3 transposition and I-F1 interference systems indicates the extent of PAM ambiguity in the transposition systems (Figure 4) and that extensive structural adaptations contribute to the process (Figure 5). These findings support a model where critical control features normally used by Cascade are now licensed by TniQ either directly or with the collaboration of the TnsA, TnsB, and TnsC transposition components.

TniQ regulates target-site preference

TniQ/TnsD proteins are known to have adapted to a variety of fixed attachment sites in bacteria and to programable attachment sites.[3,23,24] Prototypic Tn7 distinguishes between target

examined, over half of the transposition events in the pool with the A247Q S248N change had the PAM with C-1 (Figure 5C).

Our results indicate that the PAM-binding region of Cas8/5 in I-F3 CASTs has likely extensively evolved for PAM ambiguity since co-option from an ancestral canonical type I-F1 CRISPR-Cas system. Swapping the serine residue in I-F3b Cas8/5 that directly contacts the PAM −1 position to the asparagine found in I-F1 Cas8f is not sufficient to re-establish PAM CC selectivity. However, more extensive changes involving multiple residues in the PAM-binding pocket can start to re-establish the −1 C preferences suggesting rational design methods focused on the PAM-binding pocket could reconfigure PAM selectivity. Interestingly, computational modeling of the I-F1, I-F3b, and I-F3b mutants (A247Q + S248N) generally captures the experimental trends reported here (Figure S6) and suggests that successful design strategies will incorporate both flexible backbone modeling as well as careful consideration of the full PAM-binding pocket. We suggest that two important factors have been selected for PAM ambiguity in I-F3 transposition systems: capacity for privatization of chromosome-matching crRNAs from host CRISPR-Cas defense and
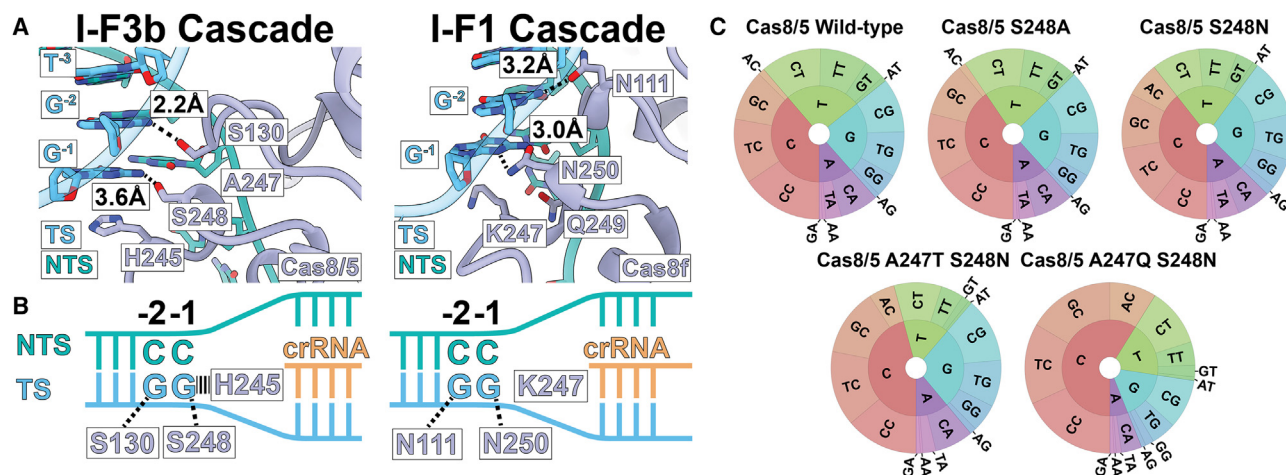
Figure 5. Structure comparison and mutation analysis indicate key residues controlling PAM discrimination

(A) Comparison of Cas8 (purple) interaction with PAM bases on the target strand (TS, blue) in the target-DNA-bound structures of I-F3b (this study, left) and I-F1 (PDB: 6NE0, right). Distances are annotated for the sequence-specific hydrogen-bonding interactions between Cas8/5 residues and DNA bases. Non-target strand (NTS) and nucleotides other than G^{-1} and G^{-2} do not form sequence-specific interactions.

(B) Cartoon diagram describing the key interactions between DNA and Cas8/5 (I-F3b, left) or Cas8f (I-F1, right).

(C) PAM wheels indicating PAM preference of I-F3b Tn6900 CAST with Cas8/5 wild type and mutants. Preference at the −1 position is represented by the inner ring; the −2 position is represented by the outer ring. Although S248A, S248N, and A247T + S248N mutants showed a modest change, A247Q + S248N mutation substantially increased −1 C preference.

sites using either of two proteins that function in parallel targeting pathways: one allowing sequence-specific DNA binding (TnsD, homologous to TniQ) or one recognizing specialized features of DNA replication found with mobile plasmids (TnsE).[25–27] A sister group of the I-F3 CAST elements outside of the major I-F3a and I-F3b clades, type I-D CAST elements, and two independently coopted type I-B CAST elements uses a hybrid approach halfway between prototypic Tn7 and I-F CAST elements, where pathway choice occurs via the association with one of the two separate TniQ proteins: either a sequence-specific TnsD/TniQ protein or a TniQ that functions with Cascade.[3,18,28,29]

Our work here indicates that in the I-F3 CAST systems, TniQ actively cooperates with Cascade to regulate transposition by sensing crRNA categories. This adds crucial insights into the function of TniQ, as previously it was unclear whether TniQ simply acted as a physical connector between target-site and core transposition components.[5] Not only do these findings provide a strong mechanistic basis for understanding previous studies highlighting complex regulatory behavior in I-F3b CAST[3] and related elements[24,28] but also they reveal an evolutionarily conserved role for the TniQ/TnsD protein superfamily in facilitating decision making at attachment sites.

Cascade-TniQ forms a complete R-loop, distorting the target DNA to recruit transposition proteins

Previous studies on the I-F3a target-recognition module showed that Cascade, in the absence of TniQ, can also bind target DNA.[19,30] Consistent with this, our EMSA result suggests that the initial PAM and seed recognition would be similar with and without TniQ. However, we found that the presence of TniQ promotes R-loop formation compared with Cascade alone, which forms non-specific interactions with DNA. Our cryo-EM reconstruction of Cascade-TniQ with a fully structured R-loop reveals the interaction between TniQ and the PAM-distal DNA, consistent with our ideas on how TniQ promotes R-loop formation. A recent study examining target-site engagement with I-F3a CAST components *in vivo* using ChIP-seq found that Cascade-TniQ exhibited an enrichment at the target site greater than with Cascade alone.[30] Although the TniQ effect was largely discounted in the paper, in light of our results, an alternate explanation is that TniQ contributes to higher occupancy of the target site *in vivo* by stabilizing the full R-loop conformation. A unifying model holds that the ability of TniQ to stabilize a complete R-loop that we demonstrate is an important step for licensing TnsC recruitment as the complex progresses to a full transposition integration complex.

We show that the Cascade-TniQ complex unwinds and distorts downstream of the target DNA on full R-loop formation. Extensive studies on prototypic Tn7[4] showed that DNA distortion, produced by the TniQ family protein TnsD, is a central feature in sequential recruitment of the TnsC regulator and, eventually, the transposase.[21,25] The importance of this DNA distortion is highlighted by an artificial Tn7 targeting pathway in which a distortion induced by triplex-forming DNA is sufficient to recruit TnsABC for transposition.[31] This model is further supported by a cryo-EM structure revealing that Tn7 TnsC specifically loads adjacent to a mismatched bubble in double-stranded DNA substrates.[22] Thus, we find it compelling that a DNA distortion at the PAM-distal region, created by TniQ and the helix bundle domain of Cas8/5 (Figure 3), may also serve as a signal for TnsC recruitment in I-F3 CASTs. We suggest our complete R-loop structure represents an active conformation for downstream factor recruitment with distorted DNA and TniQ in position to make simultaneous contacts with TnsC, as has been shown in the V-K CAST.[32,33] However, we expect the recruitment of other transposition components may
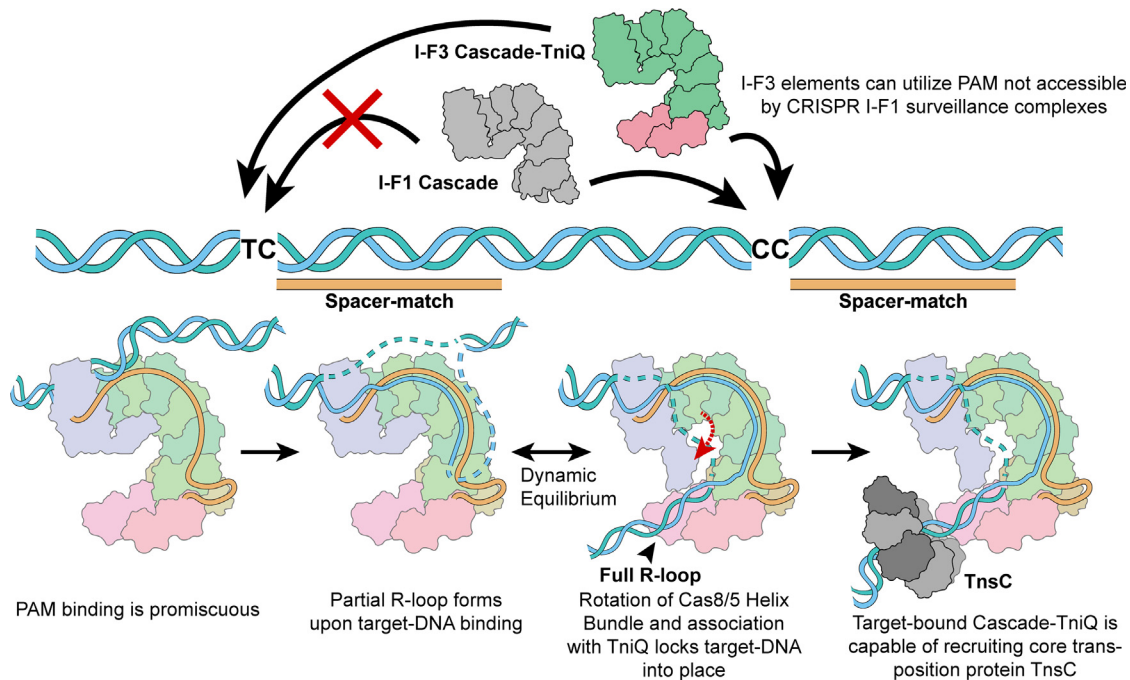
Figure 6. Schematic summarizing key mechanistic insights from this work

I-F1 CRISPR surveillance complexes (gray) have stricter PAM sequence requirements. However, the I-F3 CAST family is able to make use of loosened PAM requirements. R-loop formation is accompanied by a conformational change in the Cascade complex and locks down on target DNA via TniQ, revealing the mechanistic coupling between the CRISPR effector and core transposition protein, TniQ. This results in DNA distortions that most likely serve to recruit AAA+ regulator TnsC to direct DNA donor integration via the transposase, TnsA/B.

induce large reconfigurations as was also shown in a V-K CAST holo transposition complex.[34] Therefore, it remains an intriguing question how the rest of the transposition components recognize the DNA distortion and potentially rearrange the structure to drive transposition in a type I-F3 CAST system.

PAM ambiguity is a mechanistic adaptation of I-F3 systems, allowing attachment site drift tolerance and crRNA privatization

We speculate that PAM flexibility is important for two reasons in the I-F3 CAST transposition systems: (1) to maintain a fixed attachment site recognizable in diverse host chromosomes and (2) for privatizing attachment sites making them inaccessible to the host interference system. In fact, our experimental results extend generally to naturally occurring populations based on bioinformatics. By examining natural insertions of type I-F3b CAST elements into the native *ffs* attachment site, we find that only a small percentage (3.4%, 8/235) has the canonical CC PAM (Table S1). The vast majority of these insertions (96.6%, 227/235) utilize a TC PAM (Table S1). This indicates that PAM flexibility is an essential feature allowing these elements to recognize their chromosomal attachment site. Overall, the CC PAM is only used 4.4 % (33/757) of the time across all of the I-F3 insertion sites identified in bacterial genomes suggesting that this is a general attribute of this family of CAST elements (Table S1). Moreover, the use of a TC or other non-CC PAM attachment site would also protect chromosomal attachment sites from canonical I-F1 CRISPR-Cas inter-

ference. Type I-F3 CAST elements can naturally reside in the same host as a canonical I-F1 interference system, and it has been shown that I-F1 systems are able to use typical I-F3 CAST-encoded crRNAs for interference.[3] The TC PAM that is found 97% of the time in the *ffs* attachment site could therefore be hidden from the I-F1 system based on our interference assays, whereas this same TC PAM would be readily used for transposition (Figure 4E).

For practical applications, although, rational modification of PAM specificity would contribute to the development of orthogonally functioning, precise CAST elements. Our investigation takes one step further by establishing that extensive rearrangements must have been under selection to allow PAM ambiguity in the I-F3 systems (Figure 5). Our computational simulations suggest that accurate modeling must incorporate flexible backbone modeling of the entire PAM-binding site, not just the positions directly interacting with the PAM motif (Figure S6).

Together, these results paint a picture in which multiple adaptive changes in both the CRISPR effector (i.e., Cascade) and the associated TniQ work together to enhance the survival and distribution of CASTs. Our study demonstrates the crucial role of TniQ in the co-option of Cascade through its two important abilities: (1) it distinguishes different categories of insertion sites by sensing sequence differences in crRNAs and (2) it licenses the substrate for transposition by completing R-loop formation at the target site. These adaptations provide another exciting example of the dynamic molecular mechanisms utilized to escalate the host-parasite arms race.

Table 1. Cryo-EM data collection, refinement, and validation statistics

Name	Cascade-TniQ with atypical crRNA, full R-loop	Cascade-TniQ with atypical crRNA, partial R-loop
PDB ID	PDB: 7U5D	PDB: 7U5E
EMDB ID	EMD-26348	EMD-26349
Data collection and processing		
Microscope	Titan Krios	Titan Krios
Voltage (keV)	300	300
Camera	K3	K3
Magnification	105,000	105,000
Pixel size at detector (Å/pixel)	0.873	0.873
Total electron exposure (e$^-$/Å^2)	60	60
Exposure rate (e$^-$/pixel/s)	10.89	10.89
Number of frames collected	60	60
Defocus range (μm)	−1.0 to −2.5	−1.0 to −2.5
Automation software	SerialEM	SerialEM
Energy filter slit width	20 eV	20 eV
Micrographs collected (no.)	13,800	13,800
Micrographs used (no.)	12,024	12,024
Total extracted particles (no.)	1,338,135	1,338,135
For each reconstruction		
Refined particles (no.)	126,320	126,320
Final particles (no.)	53,353	34,800
Symmetry	C1	C1
Resolution (global, Å)		
FSC 0.5 (unmasked/masked)	7.48/4.17	8.94/4.95
FSC 0.143 (unmasked/masked)	4.26/3.52	4.95/4.03
Resolution range (local, Å)	3.3–7.0	3.4–7.0
Resolution range due to anisotropy (Å)	3.30–3.86	3.78–4.64
Map sharpening B factor (Å^2)	−70	−81
Map sharpening methods	RELION	RELION
Model composition		
Protein residues	3,603	3,474
Ligands	0	0
RNA/DNA	141	100
Model refinement		
Refinement package	Coot/Rosetta/Phenix	Coot/Rosetta/Phenix
Real or reciprocal space	Real	Real
Resolution cutoff (Å)	3.5	4.0
Model-map scores		
CC (box)	0.81	0.77
Average FSC (0.5 cutoff, Å)	3.71	4.30
RMSDs from ideal values		

Table 1. *Continued*

Name	Cascade-TniQ with atypical crRNA, full R-loop	Cascade-TniQ with atypical crRNA, partial R-loop
Bond length (Å)	0.012	0.012
Bond angles (°)	1.613	1.616
Validation		
MolProbity score	1.74	1.78
CaBLAM outliers (%)	2.15	2.26
Clashscore	10.15	11.26
Poor rotamers (%)	0.20	0.14
C-beta outliers (%)	0.03	0.03
EMRinger score	2.90	2.06
Ramachandran plot		
Favored (%)	96.66	96.66
Outliers (%)	0.17	0.12

Limitations of the study

In this study, we showed that TniQ categorizes crRNAs to regulate transposition pathway choice. Although our structures of the Cascade-TniQ complex provide key insights into the residues responsible for regulation, it remains unclear how the crRNA sequence directly impacts transposition activity. A deeper understanding of this mechanism may require more than just snapshots of the complex in certain states and may involve the kinetics of Cascade-TniQ complex assembly or target-DNA engagement. It is also possible that the crRNA sequence may affect downstream steps with the recruitment of the TnsA and TnsB transposase components. Further biochemical and structural characterizations would be required to fully understand the molecular basis of the crRNA categorization.

STAR★METHODS

Detailed methods are provided in the online version of this paper and include the following:

- KEY RESOURCES TABLE
- RESOURCE AVAILABILITY
    - Lead contact
    - Materials availability
    - Data and code availability
- EXPERIMENTAL MODEL AND STUDY PARTICIPANT DETAILS
- METHOD DETAILS
    - Protein purification
    - DNA substrate preparation
    - Electrophoretic mobility shift assay
    - Cryo-EM sample preparation and imaging
    - Image processing
    - Model building and validation
    - Rosetta refinement
    - Rosetta simulation of PAM specificity
    - Plasmid construction

CellPress

Molecular Cell
Article

- ○ Mate-out transposition assay
- ○ *P. aeruginosa* CRISPR interference assay
- ○ Randomized PAM transposition and interference assay
- ○ Cas8/5 consensus sequence logo
- QUANTIFICATION AND STATISTICAL ANALYSIS

SUPPLEMENTAL INFORMATION

Supplemental information can be found online at https://doi.org/10.1016/j.molcel.2023.05.005.

ACKNOWLEDGMENTS

This work was supported by NIH grants R00-GM124463 (E.H.K.), R01GM129118 and R21AI148941 (J.E.P.), and GM118174 (A.K.). We thank the Cornell Center for Materials Research facility as well as K. Spoth and M. Silvestry-Ramos for the maintenance of electron microscopes used for this research (NSF MRSEC program, DMR-1719875); XSEDE for computational resources used for image processing (MCB200090 to E.H.K.).

AUTHOR CONTRIBUTIONS

G.S., J.B., and S.-C.H. designed and optimized Cascade-TniQ expression conditions for complex purification. J.-U.P. performed cryo-EM. J.-U.P. and E.M. completed data collection, image processing, 3DVA, and map refinement. J.-U.P. and E.M. completed model building and map interpretation. J.B. and G.S. designed and optimized R-loop EMSA assays. V.H.T. performed PAM specificity computations with help from S.B.T. M.T.P. performed transposition assays and I-F3 CAST PAM screening. S.-C.H. performed interference assays and I-F1 CRISPR-Cas PAM screening. A.K., E.H.K., and J.E.P. oversaw all aspects of work in their laboratories. J.-U.P., E.M., and M.T.P. made figures and J.-U.P., E.M., M.T.P., E.H.K., and J.E.P. drafted initial sections. A.K., E.H.K., and J.E.P. synthesized ideas from the authors and finalized the manuscript.

DECLARATION OF INTERESTS

Cornell University has filed patent applications related to this system with M.T.P., J.E.P., and E.H.K. as inventors. The J.E.P. lab has corporate funding for research that is not directly related to the work in this publication.

Received: March 11, 2022
Revised: February 23, 2023
Accepted: May 3, 2023
Published: June 1, 2023

REFERENCES

1. Anzalone, A.V., Koblan, L.W., and Liu, D.R. (2020). Genome editing with CRISPR-Cas nucleases, base editors, transposases and prime editors. Nat. Biotechnol. *38*, 824–844. https://doi.org/10.1038/s41587-020-0561-9.

2. Peters, J.E. (2019). Targeted transposition with Tn7 elements: safe sites, mobile plasmids, CRISPR/Cas and beyond. Mol. Microbiol. *112*, 1635–1644. https://doi.org/10.1111/mmi.14383.

3. Petassi, M.T., Hsieh, S.C., and Peters, J.E. (2020). Guide RNA categorization enables target site choice in Tn7-CRISPR-Cas transposons. Cell *183*, 1757–1771.e18. https://doi.org/10.1016/j.cell.2020.11.005.

4. Peters, J.E. (2015). Tn7. In Mobile DNA, *III*, L.C. Nancy, P. Rice, A. Lambowitz, M. Gellert, and S.B. Sandmeyer, eds. (ASM Press).

5. Halpin-Healy, T.S., Klompe, S.E., Sternberg, S.H., and Fernández, I.S. (2020). Structural basis of DNA targeting by a transposon-encoded CRISPR-Cas system. Nature *577*, 271–274. https://doi.org/10.1038/s41586-019-1849-0.

6. Wang, B., Xu, W., and Yang, H. (2020). Structural basis of a Tn7-like transposase recruitment and DNA loading to CRISPR-Cas surveillance complex. Cell Res. *30*, 185–187.

7. Li, Z., Zhang, H., Xiao, R., and Chang, L. (2020). Cryo-EM structure of a type IF CRISPR RNA guided surveillance complex bound to transposition protein TniQ. Cell Res. *30*, 179–181.

8. Jia, N., Xie, W., de la Cruz, M.J., Eng, E.T., and Patel, D.J. (2020). Structure-function insights into the initial step of DNA integration by a CRISPR-Cas-Transposon complex. Cell Res. *30*, 182–184. https://doi.org/10.1038/s41422-019-0272-2.

9. Punjani, A., and Fleet, D.J. (2021). 3D variability analysis: resolving continuous flexibility and discrete heterogeneity from single particle cryo-EM. J. Struct. Biol. *213*, 107702. https://doi.org/10.1016/j.jsb.2021.107702.

10. Rollins, M.F., Chowdhury, S., Carter, J., Golden, S.M., Miettinen, H.M., Santiago-Frangos, A., Faith, D., Lawrence, C.M., Lander, G.C., and Wiedenheft, B. (2019). Structure reveals a mechanism of CRISPR-RNA-guided nuclease recruitment and anti-CRISPR viral mimicry. Mol. Cell *74*, 132–142.e5. https://doi.org/10.1016/j.molcel.2019.02.001.

11. Sharpe, P.L., and Craig, N.L. (1998). Host proteins can stimulate Tn7 transposition: a novel role for the ribosomal protein L29 and the acyl carrier protein. EMBO J. *17*, 5822–5831. https://doi.org/10.1093/emboj/17.19.5822.

12. Schmitz, M., Querques, I., Oberli, S., Chanez, C., and Jinek, M. (2022). Structural basis for the assembly of the type V CRISPR-associated transposon complex. Cell *185*, 4999–5010.e17. https://doi.org/10.1016/j.cell.2022.11.009.

13. Rollins, M.F., Schuman, J.T., Paulus, K., Bukhari, H.S., and Wiedenheft, B. (2015). Mechanism of foreign DNA recognition by a CRISPR RNA-guided surveillance complex from Pseudomonas aeruginosa. Nucleic Acids Res. *43*, 2216–2222. https://doi.org/10.1093/nar/gkv094.

14. Rybarski, J.R., Hu, K., Hill, A.M., Wilke, C.O., and Finkelstein, I.J. (2021). Metagenomic discovery of CRISPR-associated transposons. Proc. Natl. Acad. Sci. USA *118*, e2112279118. https://doi.org/10.1073/pnas.2112279118.

15. Vo, P.L.H., Ronda, C., Klompe, S.E., Chen, E.E., Acree, C., Wang, H.H., and Sternberg, S.H. (2021). Crispr RNA-guided integrases for high-efficiency, multiplexed bacterial genome engineering. Nat. Biotechnol. *39*, 480–489. https://doi.org/10.1038/s41587-020-00745-y.

16. Yang, S., Zhang, Y., Xu, J., Zhang, J., Zhang, J., Yang, J., Jiang, Y., and Yang, S. (2021). Orthogonal CRISPR-associated transposases for parallel and multiplexed chromosomal integration. Nucleic Acids Res. *49*, 10192–10202. https://doi.org/10.1093/nar/gkab752.

17. Klompe, S.E., Vo, P.L.H., Halpin-Healy, T.S., and Sternberg, S.H. (2019). Transposon-encoded CRISPR-Cas systems direct RNA-guided DNA integration. Nature *571*, 219–225. https://doi.org/10.1038/s41586-019-1323-z.

18. Klompe, S.E., Jaber, N., Beh, L.Y., Mohabir, J.T., Bernheim, A., and Sternberg, S.H. (2022). Evolutionary and mechanistic diversity of Type I-F CRISPR-associated transposons. Mol. Cell *82*, 616–628.e5. https://doi.org/10.1016/j.molcel.2021.12.021.

19. Wimmer, F., Mougiakos, I., Englert, F., and Beisel, C.L. (2022). Rapid cell-free characterization of multi-subunit CRISPR effectors and transposons. Mol. Cell *82*, 1210–1224.e6. https://doi.org/10.1016/j.molcel.2022.01.026.

20. Luscombe, N.M., Laskowski, R.A., and Thornton, J.M. (2001). Amino acid-base interactions: a three-dimensional analysis of protein-DNA interactions at an atomic level. Nucleic Acids Res. *29*, 2860–2874. https://doi.org/10.1093/nar/29.13.2860.

21. Kuduvalli, P.N., Rao, J.E., and Craig, N.L. (2001). Target DNA structure plays a critical role in Tn7 transposition. EMBO J. *20*, 924–932.

22. Shen, Y., Gomez-Blanco, J., Petassi, M.T., Peters, J.E., Ortega, J., and Guarné, A. (2022). Structural basis for DNA targeting by the Tn7 transposon. Nat. Struct. Mol. Biol. *29*, 143–151. https://doi.org/10.1038/s41594-022-00724-8.

1836 Molecular Cell *83*, 1827–1838, June 1, 2023

23. Peters, J.E., Makarova, K.S., Shmakov, S., and Koonin, E.V. (2017). Recruitment of CRISPR-Cas systems by Tn7-like transposons. Proc. Natl. Acad. Sci. USA *114*, E7358–E7366. https://doi.org/10.1073/pnas.1709035114.

24. Hsieh, S.-C., and Peters, J.E. (2021). Tn7-CRISPR-Cas12K elements manage pathway choice using truncated repeat-spacer units to target tRNA attachment sites. https://doi.org/10.1101/2021.02.06.429022.

25. Mitra, R., McKenzie, G.J., Yi, L., Lee, C.A., and Craig, N.L. (2010). Characterization of the TnsD-attTn7 complex that promotes site-specific insertion of Tn7. Mobile DNA *1*, 18. https://doi.org/10.1186/1759-8753-1-18.

26. Shi, Q., Straus, M.R., Caron, J.J., Wang, H., Chung, Y.S., Guarné, A., and Peters, J.E. (2015). Conformational toggling controls target site choice for the heteromeric transposase element Tn7. Nucleic Acids Res. *43*, 10734–10745. https://doi.org/10.1093/nar/gkv913.

27. Parks, A.R., Li, Z., Shi, Q., Owens, R.M., Jin, M.M., and Peters, J.E. (2009). Transposition into replicating DNA occurs through interaction with the processivity factor. Cell *138*, 685–695.

28. Saito, M., Ladha, A., Strecker, J., Faure, G., Neumann, E., Altae-Tran, H., Macrae, R.K., and Zhang, F. (2021). Dual modes of CRISPR-associated transposon homing. Cell *184*, 2441–2453.e18. https://doi.org/10.1016/j.cell.2021.03.006.

29. Hsieh, S.-C., and Peters, J.E. (2022). Discovery and characterization of novel type I-D CRISPR-guided transposons identified among diverse Tn7-like elements in cyanobacteria. Nucleic Acids Res. *15*, 765–782. https://doi.org/10.1093/nar/gkac1216.

30. Hoffmann, F.T., Kim, M., Beh, L.Y., Wang, J., Vo, P.L.H., Gelsinger, D.R., George, J.T., Acree, C., Mohabir, J.T., Fernández, I.S., et al. (2022). Selective TnsC recruitment enhances the fidelity of RNA-guided transposition. Nature *609*, 384–393. https://doi.org/10.1038/s41586-022-05059-4.

31. Rao, J.E., Miller, P.S., and Craig, N.L. (2000). Recognition of triple-helical DNA structures by transposon Tn7. Proc. Natl. Acad. Sci. USA *97*, 3936–3941.

32. Park, J.U., Tsai, A.W., Mehrotra, E., Petassi, M.T., Hsieh, S.C., Ke, A., Peters, J.E., and Kellogg, E.H. (2021). Structural basis for target site selection in RNA-guided DNA transposition systems. Science *373*, 768–774. https://doi.org/10.1126/science.abi8976.

33. Querques, I., Schmitz, M., Oberli, S., Chanez, C., and Jinek, M. (2021). Target site selection and remodelling by type V CRISPR-transposon systems. Nature *599*, 497–502. https://doi.org/10.1038/s41586-021-04030-z.

34. Park, J.U., Tsai, A.W., Rizo, A.N., Truong, V.H., Wellner, T.X., Schargel, R.D., and Kellogg, E.H. (2023). Structures of the holo CRISPR RNA-guided transposon integration complex. Nature *613*, 775–782. https://doi.org/10.1038/s41586-022-05573-5.

35. Tegunov, D., and Cramer, P. (2019). Real-time cryo-electron microscopy data preprocessing with Warp. Nat. Methods *16*, 1146–1152. https://doi.org/10.1038/s41592-019-0580-y.

36. Punjani, A., Rubinstein, J.L., Fleet, D.J., and Brubaker, M.A. (2017). cryoSPARC: algorithms for rapid unsupervised cryo-EM structure determination. Nat. Methods *14*, 290–296. https://doi.org/10.1038/nmeth.4169.

37. Bepler, T., Morin, A., Rapp, M., Brasch, J., Shapiro, L., Noble, A.J., and Berger, B. (2019). Positive-unlabeled convolutional neural networks for particle picking in cryo-electron micrographs. Nat. Methods *16*, 1153–1160. https://doi.org/10.1038/s41592-019-0575-8.

38. Scheres, S.H. (2012). RELION: implementation of a Bayesian approach to cryo-EM structure determination. J. Struct. Biol. *180*, 519–530. https://doi.org/10.1016/j.jsb.2012.09.006.

39. Pettersen, E.F., Goddard, T.D., Huang, C.C., Couch, G.S., Greenblatt, D.M., Meng, E.C., and Ferrin, T.E. (2004). UCSF Chimera–a visualization system for exploratory research and analysis. J. Comput. Chem. *25*, 1605–1612. https://doi.org/10.1002/jcc.20084.

40. Goddard, T.D., Huang, C.C., Meng, E.C., Pettersen, E.F., Couch, G.S., Morris, J.H., and Ferrin, T.E. (2018). UCSF ChimeraX: meeting modern challenges in visualization and analysis. Protein Sci. *27*, 14–25. https://doi.org/10.1002/pro.3235.

41. Yang, J., and Zhang, Y. (2015). I-TASSER server: new development for protein structure and function predictions. Nucleic Acids Res. *43*, W174–W181. https://doi.org/10.1093/nar/gkv342.

42. Emsley, P., Lohkamp, B., Scott, W.G., and Cowtan, K. (2010). Features and development of coot. Acta Crystallogr. D Biol. Crystallogr. *66*, 486–501. https://doi.org/10.1107/S0907444910007493.

43. Frenz, B., Walls, A.C., Egelman, E.H., Veesler, D., and DiMaio, F. (2017). RosettaES: a sampling strategy enabling automated interpretation of difficult cryo-EM maps. Nat. Methods *14*, 797–800. https://doi.org/10.1038/nmeth.4340.

44. Williams, C.J., Headd, J.J., Moriarty, N.W., Prisant, M.G., Videau, L.L., Deis, L.N., Verma, V., Keedy, D.A., Hintze, B.J., Chen, V.B., et al. (2018). MolProbity: more and better reference data for improved all-atom structure validation. Protein Sci. *27*, 293–315. https://doi.org/10.1002/pro.3330.

45. Afonine, P.V., Klaholz, B.P., Moriarty, N.W., Poon, B.K., Sobolev, O.V., Terwilliger, T.C., Adams, P.D., and Urzhumtsev, A. (2018). New tools for the analysis and validation of cryo-EM maps and atomic models. Acta Crystallogr. D Struct. Biol. *74*, 814–840. https://doi.org/10.1107/S2059798318009324.

46. Cock, P.J., Antao, T., Chang, J.T., Chapman, B.A., Cox, C.J., Dalke, A., Friedberg, I., Hamelryck, T., Kauff, F., Wilczynski, B., and de Hoon, M.J. (2009). Biopython: freely available Python tools for computational molecular biology and bioinformatics. Bioinformatics *25*, 1422–1423. https://doi.org/10.1093/bioinformatics/btp163.

47. Hunter, J.D. (2007). Matplotlib: A 2D graphics environment. Comput. Sci. Eng. *9*, 90–95.

48. Waskom, M.L. (2021). Seaborn: statistical data visualization. J. Open Source Software *6*, 3021.

49. Ondov, B.D., Bergman, N.H., and Phillippy, A.M. (2011). Interactive metagenomic visualization in a Web browser. BMC Bioinformatics *12*, 385.

50. Crooks, G.E., Hon, G., Chandonia, J.M., and Brenner, S.E. (2004). WebLogo: a sequence logo generator. Genome Res. *14*, 1188–1190. https://doi.org/10.1101/gr.849004.

51. Li, W., and Godzik, A. (2006). Cd-hit: a fast program for clustering and comparing large sets of protein or nucleotide sequences. Bioinformatics *22*, 1658–1659. https://doi.org/10.1093/bioinformatics/btl158.

52. Edgar, R.C. (2004). MUSCLE: multiple sequence alignment with high accuracy and high throughput. Nucleic Acids Res. *32*, 1792–1797. https://doi.org/10.1093/nar/gkh340.

53. Zivanov, J., Nakane, T., and Scheres, S.H.W. (2019). A Bayesian approach to beam-induced motion correction in cryo-EM single-particle analysis. IUCrJ *6*, 5–17. https://doi.org/10.1107/S205225251801463X.

54. Zivanov, J., Nakane, T., Forsberg, B.O., Kimanius, D., Hagen, W.J., Lindahl, E., and Scheres, S.H. (2018). New tools for automated high-resolution cryo-EM structure determination in RELION-3. eLife *7*, e42166. https://doi.org/10.7554/eLife.42166.

55. Echols, N., Grosse-Kunstleve, R.W., Afonine, P.V., Bunkóczi, G., Chen, V.B., Headd, J.J., McCoy, A.J., Moriarty, N.W., Read, R.J., Richardson, D.C., et al. (2012). Graphical tools for macromolecular crystallography in PHENIX. J. Appl. Crystallogr. *45*, 581–586. https://doi.org/10.1107/S0021889812017293.

56. Kuhlman, B., Dantas, G., Ireton, G.C., Varani, G., Stoddard, B.L., and Baker, D. (2003). Design of a novel globular protein fold with atomic-level accuracy. Science *302*, 1364–1368. https://doi.org/10.1126/science.1089427.

57. Dantas, G., Kuhlman, B., Callender, D., Wong, M., and Baker, D. (2003). A large scale test of computational protein design: folding and stability of nine completely redesigned globular proteins. J. Mol. Biol. *332*, 449–460. https://doi.org/10.1016/S0022-2836(03)00888-X.

58. Hu, X., Wang, H., Ke, H., and Kuhlman, B. (2007). High-resolution design of a protein loop. Proc. Natl. Acad. Sci. USA *104*, 17668–17673. https://doi.org/10.1073/pnas.0707977104.

59. Leaver-Fay, A., Kuhlman, B., and Snoeyink, J. (2005). An adaptive dynamic programming algorithm for the side chain placement problem. Pac. Symp. Biocomput. *10*, 16–27.

60. Fleishman, S.J., Leaver-Fay, A., Corn, J.E., Strauch, E.M., Khare, S.D., Koga, N., Ashworth, J., Murphy, P., Richter, F., Lemmon, G., et al. (2011). RosettaScripts: a scripting language interface to the Rosetta macromolecular modeling suite. PLoS One *6*, e20161. https://doi.org/10.1371/journal.pone.0020161.

61. Ashworth, J., Taylor, G.K., Havranek, J.J., Quadri, S.A., Stoddard, B.L., and Baker, D. (2010). Computational reprogramming of homing endonuclease specificity at multiple adjacent base pairs. Nucleic Acids Res. *38*, 5601–5608. https://doi.org/10.1093/nar/gkq283.

62. Thyme, S.B., Jarjour, J., Takeuchi, R., Havranek, J.J., Ashworth, J., Scharenberg, A.M., Stoddard, B.L., and Baker, D. (2009). Exploitation of binding energy for catalysis and design. Nature *461*, 1300–1304. https://doi.org/10.1038/nature08508.

63. Ashworth, J., and Baker, D. (2009). Assessment of the optimization of affinity and specificity at protein-DNA interfaces. Nucleic Acids Res. *37*, e73. https://doi.org/10.1093/nar/gkp242.

64. Ashworth, J., Havranek, J.J., Duarte, C.M., Sussman, D., Monnat, R.J., Jr., Stoddard, B.L., and Baker, D. (2006). Computational redesign of endonuclease DNA binding and cleavage specificity. Nature *441*, 656–659. https://doi.org/10.1038/nature04818.

65. Alford, R.F., Leaver-Fay, A., Jeliazkov, J.R., O'Meara, M.J., DiMaio, F.P., Park, H., Shapovalov, M.V., Renfrew, P.D., Mulligan, V.K., Kappel, K., et al. (2017). The Rosetta all-atom energy function for macromolecular modeling and design. J. Chem. Theor. Comput. *13*, 3031–3048. https://doi.org/10.1021/acs.jctc.7b00125.

66. Peters, J.E. (2007). Gene transfer in Gram-negative bacteria. In Methods for General and Molecular Microbiology, C.A. Reddy, T.J. Beveridge, J.A. Breznak, G.A. Marzluf, T.M. Schmidt, and L.R. Snyder, eds. (ASM Press). https://doi.org/10.1128/9781555817497.ch31.

67. Leenay, R.T., Maksimchuk, K.R., Slotkowski, R.A., Agrawal, R.N., Gomaa, A.A., Briner, A.E., Barrangou, R., and Beisel, C.L. (2016). Identifying and visualizing functional PAM diversity across CRISPR-Cas systems. Mol. Cell *62*, 137–147.

68. Fu, L., Niu, B., Zhu, Z., Wu, S., and Li, W. (2012). CD-HIT: accelerated for clustering the next-generation sequencing data. Bioinformatics *28*, 3150–3152. https://doi.org/10.1093/bioinformatics/bts565.

STAR★METHODS

KEY RESOURCES TABLE

REAGENT or RESOURCE	SOURCE	IDENTIFIER
Bacterial and virus strains		
Escherichia coli DH5α	J. Peters Lab	N/A
Escherichia coli BW27783 *attTn7*::miniTn7(miniTn6900(kanR))	J. Peters Lab, Pettasi et al., 2020[3]	MTP997
Escherichia coli BL21-AI	Invitrogen	Cat# C607003
Escherichia coli CW51	J. Peters Lab	JP606
T7 Express Competent *Escherichia coli*	NEB	Cat# C2566H
Critical commercial assays		
Q5® High-Fidelity DNA polymerase	NEB	Cat# M0491L
NEBuilder® HiFi DNA Assembly Master Mix	NEB	Cat# E2621L
His-Pur™ Ni-NTA resin	ThermoFisher	Cat# 88221
CloneJET PCR Cloning Kit	ThermoFisher	Cat# K1231
GeneJET Gel Extraction Kit	ThermoFisher	Cat# K0691
T4 DNA Ligase	ThermoFisher	Cat# EL0011
Deposited data		
Full R-loop Cascade-TniQ complex	This paper	PDB: 7U5D EMDB: 26348
Partial R-loop Cascade-TniQ complex	This paper	PDB: 7U5E EMDB: 26349
Custom code for Rosetta simulations and PAM analyses and plots	This paper	Mendeley data: https://doi.org/ 10.17632/gjgspgnxvy.1
NGS data for PAM analysis	This paper, NCBI Sequence Read Archive	Bioproject: PRJNA935286
Oligonucleotides		
Oligo_cryo1, CCGCAAGAGGATGATTCG GGTGCTTACCTCCTGACCTTCTTTAGTAG GTTCAACCCCTGATCGAGTGCCGGGATGT	This paper	N/A
Oligo_cryo2, TGGCCCCATCAGCCACATCCCGG CACTCGAAGTCCCCAACTTGGATG ATTTCTTCCAGTCCTGGTAAGCAC CCGAATCATCCTCTTGCGG	This paper	N/A
Oligo_cryo3, GGCTGATGGGGCCACCACCT TGCGCTCGTTCGCCAGCCAG	This paper	N/A
Oligo_cryo4, CTGGCTGGCGAACGAGCGCAAGGTGG	This paper	N/A
F_EMSA, ACCTGCAGGCATGCAAG	This paper	N/A
R_EMSA, /Cy5/GCAGTTAAGTGCCTG CTGGCGAGGAAGCGGAAGAG	This paper	N/A
DNA substrate for EMSA, Top_ffs_bubble_EMSA Cy3/GCGGCACAGGTCTCACGCGTTCGTCACTAC CAGGACTGGAAGAAATCATCCAAGTTGGGGACT TCGAGTGCCGGGATGTGGCTGATGGGGCCACC ACCTGTTTCTGCACTTCAACCAGTTAGCCT CCAGAGCAACCGAGACCCGCTGCTG	This paper	N/A
DNA substrate for EMSA, Bottom_ffs_bubble_EMSA CAGCAGCGGGTCTCGGTTGCTCTGGAGGCTAACT GGTTGAAGTGCAGAAACAGGTGGTGGCCCCATCA GCCACATCCCGGCACTCGATTATTTTTTTTAATTTAT TAAATAATTTTATTAGGTAGTGACGAACGCGTGAG ACCTGTGCCGC	This paper	N/A

(Continued on next page)

Continued		
REAGENT or RESOURCE	SOURCE	IDENTIFIER
Recombinant DNA		
All plasmids used and constructed in this study	This paper	See Table S2
Software and algorithms		
Warp	Tegunov et al.[35]	http://www.warpem.com/warp/
cryoSPARC	Punjani et al.[36]	https://cryosparc.com/
Topaz	Bepler et al.[37]	https://cb.csail.mit.edu/cb/topaz/
RELION	Scheres[38]	https://relion.readthedocs.io/en/release-4.0/
cryoSPARC 3DVA	Punjani et al.[9]	https://cryosparc.com/
UCSF Chimera	Pettersen et al.[39]	https://www.cgl.ucsf.edu/chimera/
UCSF ChimeraX	Goddard et al.[40]	https://www.cgl.ucsf.edu/chimerax/
I-TASSER	Yang et al.[41]	https://zhanggroup.org/I-TASSER/
Coot	Emsley et al.[42]	https://www2.mrc-lmb.cam.ac.uk/personal/pemsley/coot/
RosettaES	Frenz et al.[43]	https://dimaiolab.ipd.uw.edu/software/
MolProbity	Williams et al.[44]	http://molprobity.biochem.duke.edu/
Phenix	Afonine et al.[45]	https://phenix-online.org/
Biopython	Cock et al.[46]	https://biopython.org/
Matplotlib	Hunter[47]	https://matplotlib.org/
Seaborn	Waskom[48]	https://seaborn.pydata.org/
Krona	Ondov et al.[49]	https://github.com/marbl/Krona/wiki
WebLogo 3	Crooks et al.[50]	http://weblogo.threeplusone.com/
Cd-hit	Li et al.[51]	https://github.com/weizhongli/cdhit
MUSCLE	Edgar[52]	http://www.drive5.com/muscle
APBS	Jurrus et al. https://doi.org/10.1002/pro.3280. PMID: 28836357; PMCID: PMC5734301.	https://server.poissonboltzmann.org/apbs

RESOURCE AVAILABILITY

Lead contact
Further information and requests for resources and reagents should be directed to and will be fulfilled by lead contact, Joseph E. Peters (joe.peters@cornell.edu).

Materials availability
Newly generated materials are available from the lead contact upon reasonable request.

Data and code availability
- All data generated in this study, including atomic coordinates for Cascade-TniQ bound to target DNA for both full and partial R-loop states, have been deposited. Raw imaging data have been deposited at Mendeley data. All data are publicly available as of the date of publication. Accession numbers and DOI are listed in the key resources table.
- All original code used for analysis have been deposited at Mendeley. DOI is listed in the key resources table.
- Any additional information required to reanalyze the data reported in this paper is available from the lead contact upon request.

EXPERIMENTAL MODEL AND STUDY PARTICIPANT DETAILS

Escherichia coli strains were grown at 30 or 37°C in lysogeny broth (LB) or on LB agar (unless stated otherwise in the method details) supplemented with the following concentrations of antibiotics when appropriate: 100 μg/mL carbenicillin, 10 μg/mL gentamicin, 30 μg/mL chloramphenicol, 8 μg/mL tetracycline, 50 μg/mL kanamycin, 100 μg/mL spectinomycin.

METHOD DETAILS

Protein purification

Expression plasmid sets were transformed into *E. coli* T7 Express cells (New England Biolabs). For Cascade-TniQ for cryo-EM imaging, plasmid set was pOPO066 (pETDuet-1-*cas8/5-cas7*), pOPO097 (pACYCDuet-1-*cas6-cas7*), pOPO127 (pCOLADuet-1-His6-*tniQ*), and pGS100 (pCDFDuet_crRNA-ffsx6). For Cascade-TniQ for EMSA, plasmid set was pOPO066 (pETDuet-1-*cas8/5-cas7*), pOPO097 (pA-CYCDuet-1-*cas6-cas7*), pOPO127 (pCOLADuet-1-His6-*tniQ*), and pMTP1277 (pCDFDuet_crRNA-ffsx6(alt)). For Cascade without TniQ for EMSA, plasmid set was pOPO065 (pETDuet-1-His6-*cas8/5-cas7*), pOPO097 (pACYCDuet-1-*cas6-cas7*), and pMTP1277 (pCDFDuet_crRNA-ffsx6(alt)). Cells were grown in LB with appropriate antibiotics at 37°C to OD_{600} 0.8 and induced overnight at 16°C with 0.4mM IPTG. Cells were pelleted, resuspended in lysis buffer (500mM NaCl 25mM HEPES pH 7.5 10% glycerol 5mM DTT) plus 1mM PMSF, and lysed by sonication. After sonication cells were centrifuged at 12,000 rpm for 45 min and the supernatant was collected and imidazole was added to a final concentration of 20mM. The supernatant was loaded to 2mL Ni-NTA resin (ThermoFisher). The Ni-NTA resin was washed with 150mL of lysis buffer with graded increases of imidazole to 50mM. Complexes were eluted from the Ni-NTA resin with lysis buffer plus 300mM imidazole. Eluted cascade complexes were then purified with anion exchange chromatography (MonoQ 5/50GL cytiva). Peak fractions were collected and snap-frozen in liquid nitrogen for later use (Figure S3A).

DNA substrate preparation

Bubbled dsDNA substrate for cryo-EM sample preparation was created by heating 4 oligonucleotides (Oligo_cryo1, Oligo_cryo2, Oligo_cryo3, Oligo_cryo4, key resources table) to 95°C for 10min in duplex buffer (30mM HEPES, pH 7.5; 100mM potassium acetate) followed by slow cooling. Annealed DNA was ligated with T4 ligase (ThemoFisher), ran on a 12% UREA-PAGE gel, and successfully ligated bands were cut and extracted from the gel. Purified ssDNA was then reannealed in duplex buffer, run on a 1% agarose gel to remove free ssDNA, and purified using GeneJet gel extraction kit (ThermoFisher).

Electrophoretic mobility shift assay

The ffs protospacer was cloned into pJET vectors (ThermoFisher). 214bp DNA target for EMSA was PCR amplified from the cloned pJET vectors using fluorescently labeled primers (F_EMSA and R_EMSA, key resources table). Serial dilutions of Cascade or Cascade-TniQ were mixed with the DNA target (0.5nM) in EMSA buffer (100mM KCl, 5% glycerol, 5mM $MgCl_2$, 2mM β-mercaptoethanol), and incubated at 37°C for 15 minutes. 20 μL of DNA binding reactions were run on a 1% agarose TBE gel for 1 hour and 15 minutes at 60 V at 4°C. The gel was imaged with an Amersham Typhoon Biomolecular Imager (GE Healthcare Life Sciences) and analyzed using ImageQuant 1D version 8.2 (GE Healthcare Life Sciences). The bubbled target was prepared using IDT ultramer oligos (Top_ffs_bubble_EMSA and Bottom_ffs_bubble_EMSA, key resources table) which were annealed and gel purified. The 214bp dsDNA target from the previous EMSA was compared with the bubbled DNA target. 500nM of Cascade-TniQ was mixed with the dsDNA target or bubbled DNA target (0.5 nM) in EMSA buffer and incubated at 37°C for 15 minutes. 20 μL of DNA binding reactions were run on a 1% agarose TBE gel for 1 hour and 15 minutes at 60 V at 4°C. The gel was imaged with a ChemiDoc imaging system (Bio-Rad).

Cryo-EM sample preparation and imaging

For the Cascade-TniQ with atypical crRNA, purified Cascade-TniQ sample was supplemented with 1.2-fold molar excess of target DNA with 32 base artificial bubble (see above). Then the Cascade-TniQ in the solution was diluted to 2 μM (~0.9 mg/mL) making the final buffer composition as follows: 25 mM HEPES pH 7.5, 150 mM NaCl. The sample was incubated for 30 minutes on ice before being vitrified using the Mark IV Vitrobot (ThermoFisher) set to 4°C and 100 % humidity. 4 μL of the reconstituted Cascade-TniQ-DNA sample is loaded on the QuantiFoil Cu 1.2/1.3 grids (QuantiFoil) that was freshly glow discharged using PELCO easiGlow (Ted Pella). Then the grids were immediately blotted for 6 seconds with blot force 6, followed by vitrification in the slurry of liquid ethane cooled with liquid nitrogen. The grids were first screened using Talos Arctica (ThermoFisher) operating at 200 kV, equipped with K3 direct electron detector (Gatan) and BioQuantum energy filter. Ice thickness, number of particles per image, and number of good squares are assessed to find the best grid for data collection. The chosen grid was imaged using Titan Krios G3 (ThermoFisher) operated at 300 kV, also equipped with K3 detector (Gatan) and BioQuantum energy filter (Gatan). The slit size of the energy filter was set to 20 eV. 13,800 micrographs were recorded at the 105,000X nominal magnification (corresponding to 0.873 Å per pixel) using 3 by 3 image shift, with the nominal defocus from -1.0 μm to -2.5 μm. Total 60 electrons were exposed per $Å^2$ during 4.2 seconds, fractionated into 60 frames.

Image processing

Warp[35] was used for beam-induced motion correction and CTF estimation of the total 13,800 movies. 12,024 Micrographs with 5 Å or higher CTF-fit resolution were imported to cryoSPARC[36] for further processing. Initial particle picking was done using template-based picking in cryoSPARC, followed by 2D classification. Resulting 38,807 particles from 2D averages with high-resolution features were used to train topaz[37] neural network. This trained network was applied to the filtered 12,024 micrographs to extract initial 1,338,135 particle picks. 2D classification was followed to remove "junk" particles, resulting in 1,075,078 particles from the selected

2D averages, which were then re-extracted using RELION[38] with Fourier-cropping (420 pixels to 128 pixels, corresponding to 2.86 Å per pixel). This particle stack was subjected to 3D classification in RELION, which yielded 237,671 particles of intact Cascade-TniQ complex. This particle stack was then re-extracted without Fourier cropping (0.873 Å per pixel), followed by non-uniform refinement and heterogeneous refinement in cryoSPARC. One resulting class (53%, 126,320 particles) from the heterogeneous refinement showed significantly stronger TniQ density, thus selected for the downstream analysis. We noticed that even after the two rounds of classifications, resulting particle stack incorporated considerable level of conformational heterogeneity.

Following the non-uniform refinement of the selected class (126,320 particles), 3D variability analysis[39] (3DVA) in cryoSPARC was used to analyze the conformational dynamics within the dataset. 3DVA visualization tool from cryoSPARC was used to cluster the input particle stack into three classes based on the identified eigenvectors and coordinates in the defined conformational space from the 3DVA. Each extreme of the space were identified as Cascade-TniQ complex with partial (28%, 34,800 particles) or full (20%, 26,306 particles) R-loop respectively, with 52% of particles in between showing disordered TniQ density. 34,800 particles that represent partial R-loop complex were then exported to RELION for Bayesian polishing,[53] and CTF refinement[54] of the complex, which resulted in 4.0 Å resolution of partial R-loop complex. In order to maximize the number of particles in the class of full R-loop complex, the earlier stack of 126,320 particles was subjected to two independent heterogeneous refinements. Each refinement job was set up using two volumes of the extreme clusters from the 3DVA eigenvector 1 and eigenvector 2, respectively. Each refinement resulted in 57% or 58% of Cascade-TniQ with full R-loop respectively, which were then merged and deduplicated. This stack of 91,051 particles was exported to RELION. Signals outside of the PAM-distal region is subtracted using the mask that includes Cas6, TniQ dimer, Cas8/5 helix bundle, and PAM-distal DNA (Figure S1B). Focused classification of the subtracted particles resulted in two major classes of PAM-distal DNA bound TniQ, but one class of high-resolution features (58%, 53,353 particles) was selected as the final particle stack for the Cascade-TniQ with full R-loop. CTF-refinement and Bayesian polishing of the particles resulted in 3.5 Å resolution of full R-loop complex. Focused refinement of the PAM-distal region resulted in 3.9 Å resolution. Final maps were sharpened using RELION postprocessing tool with automatically estimated B-factors. Local resolution estimation and filtering of the final reconstructions were done using cryoSPARC. For visualization, reconstructions from global and focused refinement were aligned and combined using UCSF Chimera[39] command 'fitmap' and 'vop maximum' respectively. Figures describing cryo-EM reconstructions and atomic models were generated using UCSF ChimeraX.[40]

Model building and validation
The atomic models for Cas8/5, Cas6, Cas7, and TniQ from a homologous Cascade-TniQ complex from V. cholerae (PDB: 6PIF)[5] were used as templates for homology models generated using the I-TASSER server.[41] These homology models were docked in the cryo-EM density map using UCSF Chimera[39] and residue registers and backbone geometries were then corrected using Coot.[42] Extended loops that could not be modeled manually due to locally poorer EM density were rebuilt into the cryo-EM density maps using RosettaES[43] and then manually refined in Coot in an iterative fashion. Refined protein models were subsequently relaxed into the EM density using Rosetta and were subjected to iterative rounds of relaxation in Rosetta and refinement in Coot to fix geometric and steric outliers identified by MolProbity[44] during model validation. crRNA and DNA strands were manually built into the cryo-EM density map using Coot with resolution sufficient to distinguish purines and pyrimidines and, thus, confirm the register of each strand. Nucleic acid models were refined into an EM map 'zoned' (using UCSF Chimera) to remove protein density and using phenix[45,55] real_space_refine subject to base-pair and stacking restraints generated by inspection. Details of the validation stats are summarized in Table 1.

Rosetta refinement
Missing loops and initial protein models were paired with a 'zoned' and sharpened map that contained only the density corresponding to a single protein subunit of the broader Cascade-TniQ complex. Extended loops spanning 3-12 residues with locally poorer EM density were deleted from the protein model using UCSF Chimera and then rebuilt iteratively using RosettaES with the Rosetta xml script. The best scoring model generated by Rosetta was manually examined in Coot and the next missing model was rebuilt in another round of RosettaES modeling. This procedure was integrated with manual inspection and model-building. The RosettaES xml script is accessible at Mendeley Data, accession info in the key resources table.

Rosetta simulation of PAM specificity
PDB models for the DNA-bound I-F1 Cascade (PDB: 6NE0)[10] and the full R-loop complex of the I-F3b system were used as inputs for specificity calculations. The model of I-F3b A247Q S248N mutant was generated from I-F3b full R-loop complex using fixbb application of the Rosetta modeling suite.[56–59] This application was used to fit an amino acid rotamer onto the fixed backbone of an input structure at specific positions. In order to generate 16 models of each system with 16 possible PAM combinations, -1 and -2 position nucleotides were substituted using the Simple Mutate tool from coot,[42] which replaces the base identity from the original model without altering other geometries. The RosettaScripts application[60] was used to both optimize binding and calculate specificity values of each system with each possible PAM sequence. For I-F1 Cascade and I-F3b optimized binding, we allowed for rotamer packing of the residues at positions 247 and 248. This protocol also sampled backbone movement of this two-residue span and the four residues flanking either side of this region (total of 10 adjacent residues) to improve positioning of the two residues with user-defined target DNA bases. Rotamer packing was specifically optimized to improve binding between the residue pair and the

PAM base pairs using a DNA-based energy function.[61–64] Total energy scores for each structure-PAM model were calculated after rotamer/backbone optimization. Total energy scores of each model were calculated using the same weight function, which considers both intra-protein interactions and protein-DNA interactions. These weights are composed of the standard Rosetta ref2015 energy function and additional optimized weights derived to optimize protein-DNA interactions.[65] The optimized weight function is included below (ST-DNA-10_11_21.wts). Ten independent optimization runs were performed for each Cas8/5-PAM combination to extensively sample conformational space. With each optimized model providing an energy score, ten energy scores were then averaged to be used as a Boltzmann energy term. The specificity of each design model was then calculated as a Boltzmann occupancy that compared the target structure against a partition function consisting of all competing PAM combinations. The command and the required files to run Rosetta scripts are accessible through Mendeley Data, see accession in key resources table, and can be generally used to determine the binding specificity of protein-DNA structural models. The 'res_nums' flag in Rosetta script file should be changed to represent the residue number to be sampled.

Plasmid construction

Plasmids for protein expression/purification, transposition and interference assays were constructed by standard methods including restriction/ligation, isothermal assembly, and golden gate cloning; sequences and source information (base vector sets for each system are available on Addgene) can be found in Table S2. F plasmid derivatives were made by recombineering as previously described.[3] The randomized 2-bp target plasmid for unbiased screening was constructed by amplification of plasmid backbone using primers with synthetic tails adding an 'NN'-*ffs* target sequence and XhoI cut sites, digestion with XhoI and self-ligation.

Mate-out transposition assay

Mate-out assays were performed in strain MTP997 with F plasmid derivative as indicated in Table S2. Cells were made competent by growing in LB media to mid-log and washing/resuspending in ice cold CaCl₂ solution[66] and transformed with pMTP1293 (TnsABC), pMTP1261 (TniQ-Cascade) or mutant derivatives, and pMTP1379 (atypical crRNA targeting *ffs*) or pMTP1382 (typical crRNA targeting *ffs*) as indicated in Table S2 onto LB agar supplemented with 100 μg/mL carbenicillin, 30 μg/mL chloramphenicol, 8 μg/mL tetracycline, and 0.2% w/v glucose. After 16 hours incubation at 37°C, several hundred transformants were washed up in M9 minimal media supplemented with 0.2% w/v maltose and diluted to a calculated OD = 0.3 in M9 maltose supplemented with 100 μg/mL carbenicillin, 30 μg/mL chloramphenicol, 8 μg/mL tetracycline, 0.2% w/v arabinose, and 100 μM IPTG to induce transposition.

After 24 hours incubation with shaking at 30°C, a portion of induced cultures were washed once and resuspended in LB supplemented with 0.2% w/v glucose. After 1.5 hours incubation at 37°C induced pools were mixed with prepared mid-log CW51 recipient strain at a ratio of 1:5 donor:recipient and incubated with gentle agitation for 90 minutes at 37°C to allow mating. Cultures were then vortexed, placed on ice, serially diluted in LB 0.2% w/v glucose, and plated on LB supplemented with 20 μg/mL nalidixic acid, 100 μg/mL rifampicin, 100 μg/mL spectinomycin, 50 μg/mL X-gal, with or without 50 μg/mL kanamycin to sample the entire transconjugant population or select for transposition respectively. Plates were incubated at 37°C for 36 hours before colonies were counted.

P. aeruginosa CRISPR interference assay

Interference assays were performed in BL21-AI. BL21-AI was made competent by standard chemical methods[66] and transformed with pOPO322 (*cas1_cas2/3*), pCsy_complex, and pOPO374 (PA14 crRNA-*ffs*) as indicated in Table S2 onto LB agar supplemented with 100 μg/mL carbenicillin, 100 μg/mL spectinomycin, 30 μg/mL chloramphenicol, and 0.2% w/v glucose. Overnight cultures grown in LB agar supplemented with 100 μg/mL carbenicillin, 100 μg/mL spectinomycin, 30 μg/mL chloramphenicol were diluted 1:50 in LB supplemented with 100 μg/mL carbenicillin, 100 μg/mL spectinomycin, 30 μg/mL chloramphenicol, 100 μM IPTG and 1 mM arabinose. Cultures were grown to OD = 0.4 before electrocompetent cells were prepared by standard methods[66] and transformed with 1 ng pOPO275 (CC-*ffs* target plasmid), alternate PAM derivative of pOPO275 or pOPO390 (non-target control). Cells were recovered in SOC at 37°C for one hour before being serially diluted and plated on LB supplemented with 100 μg/mL carbenicillin, 50 μg/mL kanamycin, 30 μg/mL chloramphenicol, and 100 μg/mL spectinomycin. Plates were incubated at 37°C for 16 hours before colonies were counted.

Randomized PAM transposition and interference assay

For Tn6900 unbiased PAM transposition screen, MTP997 (*Escherichia coli* BW27783 *attTn7*::miniTn7(miniTn6900(kanR))) transformed with pMTP1293 (TnsABC), pMTP1261 (TniQ-Cascade) or mutant derivatives, and pMTP1379 was made competent by standard chemical means[66] and transformed with pMTP1412 (NN-*ffs* target plasmid). >50,000 colonies were washed up, washed and resuspended to a calculated OD = 0.3 in M9 maltose induction media (M9 maltose supplemented with 100 μg/mL carbenicillin, 30 μg/mL chloramphenicol, 8 μg/mL tetracycline, 10 μg/mL gentamycin, 0.2% w/v arabinose, and 100 μM IPTG) and induced for 24 hours at 30°C before plasmids were purified with Omega E.Z.N.A. Plasmid DNA Mini Kit.

To remove self-targeting transposition into the guide-RNA expression vector contaminating transformations, plasmid pools were digested with EcoRI and SalI before transformation into DH5alpha. Transformed cells were plated onto LB supplemented with 10 μg/mL gentamycin and 50 μg/mL kanamycin to select for target plasmid with mini-transposon. >10,000 colonies were washed up and combined for plasmid purification. Purified plasmid was subjected to 2x151 bp read Illumina total DNA sequencing by Seqcenter/MiGS (Microbial Genome Sequencing Center).

For I-F1 PA14 CRISPR-Cas unbiased PAM interference screen, BL21-AI transformed with pOPO322 (pACYCDuet-*cas1_cas2/3*), pCsy_complex, and pOPO374 (pCDFDuet-PA14-ffs) was grown overnight in LB agar supplemented with 100 μg/mL carbenicillin, 100 μg/mL spectinomycin, 30 μg/mL chloramphenicol then diluted 1:50 in LB supplemented with 100 μg/mL carbenicillin, 100 μg/mL spectinomycin, 30 μg/mL chloramphenicol, 100 μM IPTG and 1 mM arabinose. Cultures were grown to OD = 0.4 before electrocompetent cells were prepared by standard methods and transformed with 1 ng pMTP1412 (pBBR-genR-NN*ffs*). Cells were recovered in SOC at 37°C for one hour before being plated on LB supplemented with 100 μg/mL carbenicillin, 50 μg/mL kanamycin, 30 μg/mL chloramphenicol, and 100 μg/mL spectinomycin. Plates were incubated at 37°C for 16 hours before >10,000 colonies were washed up, plasmids purified and 2x151 bp read Illumina total DNA sequencing was done by MiGS.

Reads were processed by custom python code[46] to extract and count reads containing each sequence permutation at the 2-bp PAM region for the plasmid pool before and after transposition/interference assay. Data was plotted as heatmaps using matplotlib/seaborn[47,48] and PAM wheels using Krona as previously described.[49,67] All code is available at Mendley Data, accession information in the key resources table.

Cas8/5 consensus sequence logo

The consensus sequence logos of Cas8/5 were made with WebLogo.[50] The Cas8/5 sequences were collected with the information from a previous study.[3] The protein sequences were deduplicated with CD-HIT[51,68] using a sequence identity cut-off of 0.95, then aligned with MUSCLE v3.8.31.[52] Sequences belonging to type I-F3a and I–F3b in the multiple alignments were then separated and used to make consensus sequence logos.

QUANTIFICATION AND STATISTICAL ANALYSIS

Statistical details are listed in the figure legends.